A Dual Mass Flux Framework for Boundary Layer Convection. Part II: Clouds

ROEL A. J. NEGGERS*

European Centre for Medium-Range Weather Forecasts, Reading, United Kingdom

(Manuscript received 1 October 2007, in final form 1 September 2008)

ABSTRACT

This paper presents the extension of the eddy diffusivity mass flux (EDMF) framework for turbulent transport into the statistical modeling of boundary layer clouds. The advection–diffusion decomposition that defines EDMF is projected onto the turbulent distribution as used in the statistical cloud model. Each EDMF component is thus assigned its own independent probability density function (PDF), resulting in an updraft PDF and a diffusive PDF. This double PDF system is configured and integrated in conserved variable space, with the position and orientation of each PDF determined by its unique nature. The parameterization of the associated updraft/diffusion decomposition of variance introduces close ties to the transport scheme; whereas the grid box mean variance is reconstructed using a prognostic variance budget, the variance of the updraft component is parameterized as a function of the spread among various resolved model updrafts. Individual model components and the scheme as a whole are evaluated in detail against large-eddy simulations of a number of prototype subtropical trade wind cases. The results show that various structures in cloud fraction, condensate, and variance are reproduced. The diffusive PDF acts to represent stratiform clouds; the advective PDF represents cumuliform clouds in conditionally unstable layers. This allows representation of complex scenarios in which both cloud forms occur, such as the transitional trade wind regime featuring cumulus rising into stratocumulus.

1. Introduction

The representation of clouds in general circulation models (GCMs) is still causing significant uncertainty in numerical climate and weather prediction through the associated strong impact on the earth's radiative budget (Houghton et al. 2001). The same is true for turbulent transport in the boundary layer, which controls the exchange of moist static energy and momentum between the surface and the free troposphere. Because both clouds and turbulence are subgrid processes, their impact has to be parameterized, which has been the subject of active research. Typically, transport and clouds are represented in separate schemes in GCMs. This separation potentially introduces compensating errors, masked by the tuning of adjustable parameters. These errors can be avoided by unification and integration of separate schemes, which for that reason has been a recent trend in atmospheric modeling (e.g., Lappen and Randall 2001; Golaz et al. 2002.

This study relates a similar attempt at subgrid model integration. It presents the extension of the eddy diffusivity mass flux (EDMF) framework for turbulent transport (Siebesma and Teixeira 2000; Siebesma et al. 2007) into the statistical modeling of boundary layer clouds (e.g., Sommeria and Deardorff 1977; Mellor 1977; Bougeault 1981). Such close coupling between the modeling of boundary layer transport and clouds is motivated by the idea that both are in principle generated by the same turbulent eddies. The associated eddy sizes and turnover time scales are relatively small compared to the typical time step and grid spacing of present-day weather prediction and climate models, which favors a statistical modeling approach.

The integration of the representation of clouds and transport is achieved by parameterizing both as a function of the same joint distribution, reconstructed using EDMF transport model variables. As a result, the representation of transport and clouds becomes internally consistent within the boundary layer scheme. Projection

* Current affiliation: Royal Netherlands Meteorological Institute (KNMI), De Bilt, Netherlands.

Corresponding author address: Roel A. J. Neggers, Royal Netherlands Meteorological Institute (KNMI), P.O. Box 201, De Bilt 3730 AE, Netherlands.
E-mail: roel.neggers@knmi.nl

DOI: 10.1175/2008JAS2636.1

of the advection–diffusion decomposition that defines EDMF on the turbulent distribution implies that each transport component gets its own independent probability density function (PDF), resulting in a diffusive PDF and an updraft PDF. This corresponds to a double PDF cloud scheme (Lewellen and Yoh 1993). An attractive aspect of such double PDF models is that they can theoretically render distributions with high (in principle unlimited) skewness and kurtosis. Such distributions are typical of convective layers in which the updrafts are often grouped and form an independent second mode (a bimodal distribution).

As compared to previous statistical cloud schemes, this approach has some novel aspects. First, with the double PDF reconstructed in conserved variable space (as defined by total specific humidity q_t and liquid water potential temperature θ_l), each PDF is assumed to be univariate, meaning that q_t and θ_l are assumed to be perfectly correlated. This allows parameterization of the PDF in terms of the variance of a single variable, the mean, and the covariance between q_t and θ_l. Accordingly, each PDF gets a unique position and orientation. Second, the parameterization of the variances of the double PDF introduces close ties to the transport model. The grid box mean variance is reconstructed using a budget that includes a variance transport term. The variance of the updraft PDF is parameterized as a function of the spread among various resolved model parcels, introduced into EDMF in Neggers et al. (2009, hereafter Part I) to enable representation of shallow cumulus convection. Finally, for the integration of cloud fraction and condensate associated with these PDFs the common method applied in previous single Gaussian models (Sommeria and Deardorff 1977; Mellor 1977) is used, except that it is now applied to a double PDF, making use of vector notation throughout the formulation to facilitate this procedure.

The technique is implemented into the planetary boundary layer (PBL) scheme of the Integrated Forecasting System (IFS) of the European Centre for Medium-Range Weather Forecasts (ECMWF) and evaluated against large-eddy simulation (LES) results. In section 2 the new statistical cloud scheme is formulated and evaluated offline using LES. Section 3 presents the SCM evaluation of the scheme against some prototype trade wind cloudy PBL scenarios, which are then further discussed in section 4.

2. Formulation

a. EDMF–DualM

The EDMF–DualM scheme for turbulent–convective transport that forms the foundation of the new statistical cloud scheme is described in detail in Part I of this study. In the eddy diffusivity mass flux (EDMF) approach (Siebesma and Teixeira 2000; Siebesma et al. 2007), a decomposition is made of the total turbulent flux $\overline{w'\phi'}$ of the conserved thermodynamic state variables $\phi \in \{q_t,\theta_l\}$ into an advective part by organized updrafts and a diffusive part by weaker, more random perturbations:

$$\overline{w'\phi'} = \mathcal{A}^{\mathrm{up}}\overline{w'\phi'}^{\mathrm{up}} + \mathcal{A}^{K}\overline{w'\phi'}^{K}, \tag{1}$$

where $\mathcal{A}^{\mathrm{up}}$ is the area fraction covered by the organized updrafts and $\mathcal{A}^{K}(= 1 - \mathcal{A}^{\mathrm{up}})$ is that covered by the remaining air. Based on the typically observed small values of the area fraction covered by organized updrafts, we choose $\mathcal{A}^{\mathrm{up}} = 0.1$ (see Part I). Whereas the vertical transport by the collection of smallest eddies is represented by a downgradient diffusive model (Köhler 2005), the transport by the largest updrafts is represented using an advective mass flux model. In Part I a dual mass flux model (DualM) is proposed that allows EDMF to represent shallow cumulus cloud layers that are flexibly coupled to the subcloud mixed layer:

$$\mathcal{A}^{\mathrm{up}}\overline{w'\phi'}^{\mathrm{up}} = \sum_{i=1}^{2} M_{ui}(\phi_{ui} - \bar{\phi}), \tag{2}$$

where the subscript u indicates an updraft group with i is its index number; $M_{ui} \equiv a_{ui}\, w_{ui}$ is the collective volumetric mass flux of group i, with a_{ui} being the area fraction covered by all updrafts in group $i(\mathcal{A}^{\mathrm{up}} = \sum_{i=1}^{2} a_{ui})$ and w_{ui} the collective vertical velocity of group i. The first transporting updraft group ($i = 1$) is defined to represent dry mixed layer updrafts; the second ($i = 2$) represents moist updrafts that condense and rise out of the mixed layer as shallow cumulus clouds. Their area partitioning is continuous in time to allow the reproduction of potentially gradual transitions to and from shallow cumulus. Finally, use is made of a nontransporting strong test parcel, representing the extreme tail of the PDF, which helps to define the cloud layer boundaries and the variance of the updraft ensemble.

b. PDF reconstruction

The advection–diffusion decomposition that defines EDMF is now projected onto the distribution that is used in the statistical cloud scheme. This implies that each EDMF component gets its own independent PDF, resulting in an updraft PDF and a diffusive PDF. Such partitioning is characteristic of observed distributions in convective situations, in which the updrafts are often grouped and form a distinct separate mode (e.g., Larson

et al. 2001). This makes the total distribution bimodal; unimodal PDF schemes have too few degrees of freedom to be able to reproduce such independent updraft modes and their impact on cloud fraction and condensate. For illustration an LES example for the Barbados Oceanographic and Meteorological Experiment (BOMEX) shallow cumulus case (see Table 1) is shown in Fig. 1a, displaying the organization into a weakly buoyant ''passive'' PDF and a second, positively buoyant updraft PDF.

The double PDF cloud scheme is constructed in conserved variable space, as schematically illustrated in Fig. 1b. The EDMF partitioning (1) is applied to the total PDF G, resulting in an updraft PDF G^{up} and a diffusive PDF G^K:

$$G = \mathcal{A}^{\mathrm{up}} G^{\mathrm{up}} + \mathcal{A}^K G^K. \tag{3}$$

Both PDFs are assumed to be Gaussian, a situation that was shown by Lewellen and Yoh (1993) to give representative distributions in convective situations. These PDFs are parameterized as a function of transport model variables, ensuring a close coupling between clouds and transport. For example, using vector notation $\mathbf{\Phi} = (q_t, \theta_l)$, the means of the updraft and diffusive PDF are $\overline{\mathbf{\Phi}}^{\mathrm{up}}$ and $\overline{\mathbf{\Phi}}^K$, respectively. The linear axes of the univariate joint PDFs are defined by a unit vector $\hat{v}$, with their orientation reflecting the unique character of each PDF; the updraft PDF axis $\hat{v}^{\mathrm{up}}$ is positioned on the lateral mixing line between the moist updraft state and the grid box mean state, whereas the diffusive PDF axis $\hat{v}^K$ is positioned on the zero buoyancy line, reflecting that diffusive motions are almost neutrally buoyant. The use of two univariate distributions oriented along two different lines is the main difference from the fully multivariate schemes of Mellor (1977), Lewellen and Yoh (1993), and Golaz et al. (2002).

Integrating the total cloud fraction $\mathcal{A}_c$ and total condensate $\bar{l}$ comes down to summation of the contributions by all PDFs weighted by their fractions:

$$\mathcal{A}_c = \mathcal{A}^{\mathrm{up}} f^{\mathrm{up}} + \mathcal{A}^K f^K \quad \text{and} \tag{4}$$

$$\bar{l} = \mathcal{A}^{\mathrm{up}} l^{\mathrm{up}} + \mathcal{A}^K l^K, \tag{5}$$

where f is the saturated area fraction and l the condensate associated with each PDF. Because we assume Gaussian PDFs, these contributions can be written in terms of the normalized saturation deficit Q, defined as the distance of the PDF mean $\bar{x}$ to the saturation curve along the PDF axis normalized by the width of the PDF σ_x:

$$f = \mathcal{B}(Q), \quad Q = \frac{x_{\mathrm{sat}} - \bar{x}}{\sigma_x}, \tag{6}$$

TABLE 1. Summary of the prototype PBL cases, documenting (in row order) (i) the case acronym, (ii) its full name, (iii) publications describing the field experiment, and (iv) publications describing the LES case setup. The KNMI LES model is described in detail by Cuijpers and Duynkerke (1993).

ASTEX modified
Atlantic Stratocumulus Transition Experiment
Albrecht et al. (1995)
Wyant et al. (1997) and Bretherton et al. (1999)
ATEX
Atlantic Trade Wind Experiment
Augstein et al. (1973, 1974)
Stevens et al. (2001)
BOMEX
Barbados Oceanographic and Meteorological Experiment
Holland and Rasmusson (1973) and Nitta and Esbensen (1974)
Siebesma et al. (2003)
DYCOMS2 RF01
Second Dynamics and Chemistry of Marine Stratocumulus field study
Stevens et al. (2003a,b)
Stevens et al. (2005)
RICO composite
Rain in Cumulus over the Ocean experiment
Rauber et al. (2007)
Van Zanten et al. (2009, manuscript submitted to *J. Atmos. Sci.*)

where x is the PDF axis coordinate, defined as

$$x \equiv \frac{(\mathbf{\Phi} - \overline{\mathbf{\Phi}}) \cdot \hat{v}}{\|\hat{v}\|}. \tag{7}$$

As a result, the PDF mean $\bar{x} \equiv 0$ per definition, x_{sat} is the intersection point of the PDF axis with the saturation curve, and $\mathcal{B}$ is a function giving the top fraction of the Gaussian PDF situated above x_{sat} as a function of Q (precalculated in Table 2 using the error function; see appendix A). A method for calculating the intersection point x_{sat} is described in appendix C. Concerning the integration of condensate, the variation of q_{sat} with x in the cloudy part of the PDF is not neglected; rather, it is linearized to properly account for its dependence on temperature. As illustrated by Fig. 2, in cumulus convection temperature varies significantly over the updraft PDF because of differential latent heat release and lateral mixing. Appendix B illustrates that such linearization allows us to write

$$l = f\left(\frac{\partial q_t}{\partial x} - \frac{\partial q_{\mathrm{sat}}}{\partial x}\right)_{x_{\mathrm{sat}}} (\bar{x}^f - x_{\mathrm{sat}}), \tag{8}$$

where $\bar{x}^f = \bar{x} + \mathcal{D}(Q)\ \sigma_x$, (9)

with $\mathcal{D}$ being another function expressing the mean of the top fraction f of a Gaussian PDF as a function of Q

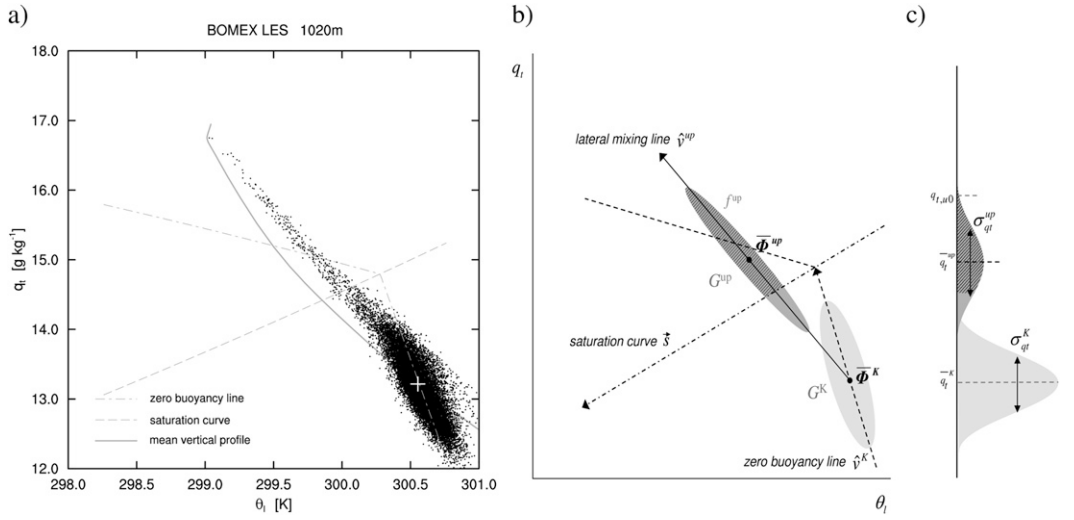

FIG. 1. (a) LES scatterplot of specific humidity and potential temperature at 1020 m during BOMEX. The gray lines represent the mean vertical profile (solid, with the white cross indicating the value at this height), the saturation curve (dashed), and the zero-buoyancy line (dashed–dotted). (b) The rendering of this distribution by the double PDF framework, including the orientation of the PDF axes $\hat{v}^{up}$ and $\hat{v}^{K}$. The diffusive PDF is light gray and the updraft PDF dark gray, of which the saturated area f^{up} is indicated by the shading. Note that for visualization the PDFs are here displayed as bivariates; however, in the model the PDFs are univariate (i.e., no variance exists orthogonal to their axes). (c) The double PDF as projected on the q_t axis.

(precalculated in Table 2). The gradients with x are estimated at x_{sat}.

c. Variance closures

It remains to determine the closure of the variance (or the square width) of each PDF. As described by Lewellen and Yoh (1993), the first and second statistical moments of a double PDF are related as

$$\bar{\phi} = \mathcal{A}^{up}\overline{\phi}^{up} + \mathcal{A}^{K}\overline{\phi}^{K} \quad \text{and} \tag{10}$$

$$\sigma_\phi^2 + \overline{\phi}^2 = \mathcal{A}^{up}(\sigma_\phi^{up2} + \overline{\phi}^{up2}) + \mathcal{A}^{K}(\sigma_\phi^{K^2} + \overline{\phi}^{K^2}), \tag{11}$$

where σ_ϕ^K and σ_ϕ^{up} express perturbations relative to means $\overline{\phi}^K$ and $\overline{\phi}^{up}$, respectively, as illustrated in Fig. 1c. These relations hold for any double PDF, not just binomial ones. The PDF fractions $\mathcal{A}^{up}$ and $\mathcal{A}^K$ and means $\overline{\phi}^{up}$ and $\overline{\phi}^K$ are provided by the transport model. It thus remains to define closure for two of the three variances in (11). We choose here to parameterize the grid box mean total variance σ_ϕ^2 and the variance among updrafts σ_ϕ^{up2}, by which the variance of the diffusive PDF σ_ϕ^K becomes a residual.

The parameter σ_x is the width of each PDF measured along the PDF axis. Because the direction of each axis is already determined, the variance of only one conserved variable is required; we choose q_t. The prognostic budget of grid box mean variance $\sigma_{q_t}^2$ consists of flux gradient production, transport, and dissipation:

$$\frac{\partial \sigma_{qt}^2}{\partial t} = -2\overline{w'q_t'}\frac{\partial \overline{q_t}}{\partial z} - \frac{\partial \overline{w'q_t'q_t'}}{\partial z} - \varepsilon, \tag{12}$$

where the horizontal flux components are neglected. In the turbulent PBL the terms on the right-hand side typically dominate over the storage term, which is neglected accordingly; this makes the budget diagnostic. All three physical processes on the right-hand side of (12) are retained and explicitly modeled. The flux in the variance production term in (12) is available from the transport model. The dissipation of variance is parameterized using a relaxation formula,

TABLE 2. The area fraction $f = \mathcal{B}(Q)$ and mean $\bar{x}^f = \bar{x} + \mathcal{D}(Q)\sigma_x$ of a top segment (as defined by normalized deficit Q) of the standard normal distribution $N(\bar{x} = 0, \sigma_x = 1)$.

Q	$\mathcal{B}(Q)$	$\mathcal{D}(Q)$	Q	$\mathcal{B}(Q)$	$\mathcal{D}(Q)$
3.719	10^{-4}	3.958	1.282	0.1	1.754
3.090	10^{-3}	3.368	0.842	0.2	1.400
2.326	0.01	2.673	0.524	0.3	1.159
2.054	0.02	2.425	0.253	0.4	0.966
1.881	0.03	2.267	0	0.5	0.798
1.751	0.04	2.153	−0.253	0.6	0.644
1.645	0.05	2.062	−0.524	0.7	0.497
1.555	0.06	1.985	−0.842	0.8	0.350
1.476	0.07	1.918	−1.282	0.9	0.195
1.405	0.08	1.859	−3.090	0.999	0.003
1.341	0.09	1.804	−∞	1.0	0

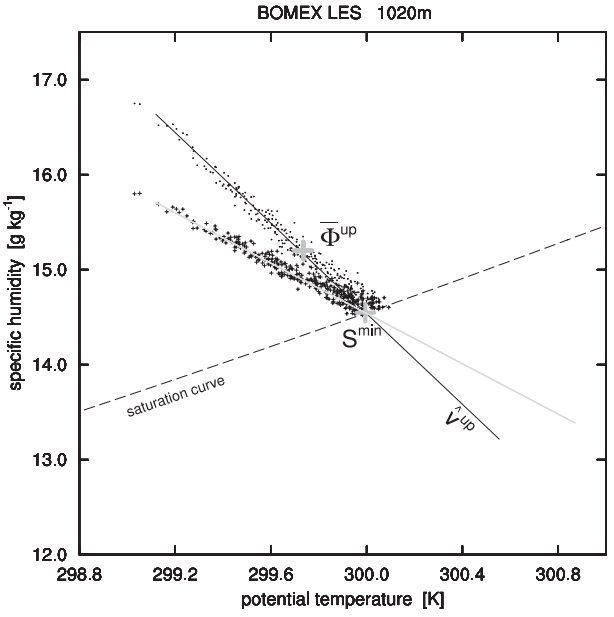

FIG. 2. As in Fig. 1, but now only showing the oversaturated $\{\theta_l, q_t\}$ points of the updraft PDF (black dots). The corresponding $\{\theta_l, q_{\text{sat}}\}$ points also shown (black plus signs), including their linear fit (gray solid line). The updraft PDF mean $\bar{\mathbf{\Phi}}^{\text{up}}$ and the minimum saturation point $\mathbf{S}^{\text{min}}$ are both marked (gray thick plus signs).

$$\varepsilon = \frac{\sigma_{qt}^2}{\tau_\sigma}, \tag{13}$$

where τ_σ is the dissipation time scale. Nieuwstadt and Brost (1986) showed that the decay time of turbulent kinetic energy and temperature variance scales with the convective turnover time scale; the same is here assumed to apply to humidity variance,

$$\tau_\sigma \approx \frac{h}{w_*}, \tag{14}$$

which is assumed to apply in the whole PBL, including the cloud layer; an argument supporting this assumption is that the convective updrafts in the cloud layer are the cloudy continuation of the strongest mixed layer updrafts that are represented by (14). Variance transport is assumed to be dominated by the strongest eddies, which motivates the use of a mass flux approach:

$$-\frac{\partial \overline{w' q_t' q_t'}}{\partial z} \approx -\frac{\partial}{\partial z} \sum_{i=1}^{2} M_{ui} (q_{t,ui} - \overline{q_t})^2. \tag{15}$$

Figure 3a shows a validation of this approach using LES. The presence of the second q_t' term dominates the vertical structure of variance transport, acting to create strong vertical gradients in $\overline{w' q_t' q_t'}$ of opposite sign near mixed layer top and cloud top. The variance transport acts to remove variance at cloud base and deposit variance near cloud top. The variance transport by the dry updraft is relatively small because large humidity excesses only occur when updrafts rise above the mixed layer top. Figure 3b shows that transport cannot be neglected in the variance budget, particularly near the top of the cumulus cloud layer.

Concerning the updraft variance $(\sigma_\phi^{\text{up}})^2$, applying the dry–moist updraft partitioning to (11) gives

$$\mathcal{A}^{\text{up}} (\sigma_\phi^{\text{up2}} + \overline{\phi}^{\text{up2}}) = \sum_{i=1}^{2} a_{ui} (\sigma_\phi^{ui^2} + \phi_{ui}^2). \tag{16}$$

Only the moist part ($i = 2$) of (16) is explicitly parameterized; the dry part ($i = 1$) is not specified but is represented indirectly by including it in the residual (diffusive) PDF (the independent treatment of the dry part is for now considered a future option). The variance among moist updrafts $(\sigma_{qt}^{u2})^2$ is obtained from the spread in properties of two model parcels representing different segments of the moist updraft PDF. For example, a larger difference will correspond to an updraft PDF that is more ''stretched'' (see Fig. 4a). In Part I the moist parcel and the strong test parcel are used to reconstruct an updraft PDF for use in the mass flux transport model; for consistency the same updraft PDF is now used in the cloud scheme as follows: The mean of the updraft PDF is positioned on the moist parcel profile $q_{t,u2}$ (as given by the single plume model). By using the precalculated function $\mathcal{D}$ the variance can then be tied to the profiles of the two parcels:

$$q_{t,\text{test}} = q_{t,u2} + \mathcal{D}(Q^{u2}) \sigma_{qt}^{u2}; \tag{17}$$

here Q^{u2} is the normalized distance between the lower boundary of the test parcel fraction and the mean of the moist updraft PDF (as illustrated in Fig. 4a),

$$Q^{u2} = \mathcal{B}^{-1} \left(\frac{a_{\text{test}}}{a_{u2}} \right). \tag{18}$$

Here superscript -1 indicates an inverse function. System (17) and (18) enables calculation of $\sigma_{q_t}^{u2}$ as a function of the various updraft fractions and means, using lookup Table 2. In practice, to avoid division by zero the updraft variance is set to zero for very small moist updraft fractions ($a_{u2} \leq 1.5\ a_{\text{test}}$). In this case, the updraft PDF corresponds to a Dirac delta function and the normalized saturation deficit in (6) reduces to a Heaviside step function. Note that the outcome of this formulation is independent of what is chosen for a_{test}. Given the PDF, a smaller a_{test} represents a smaller fraction in its tail that has

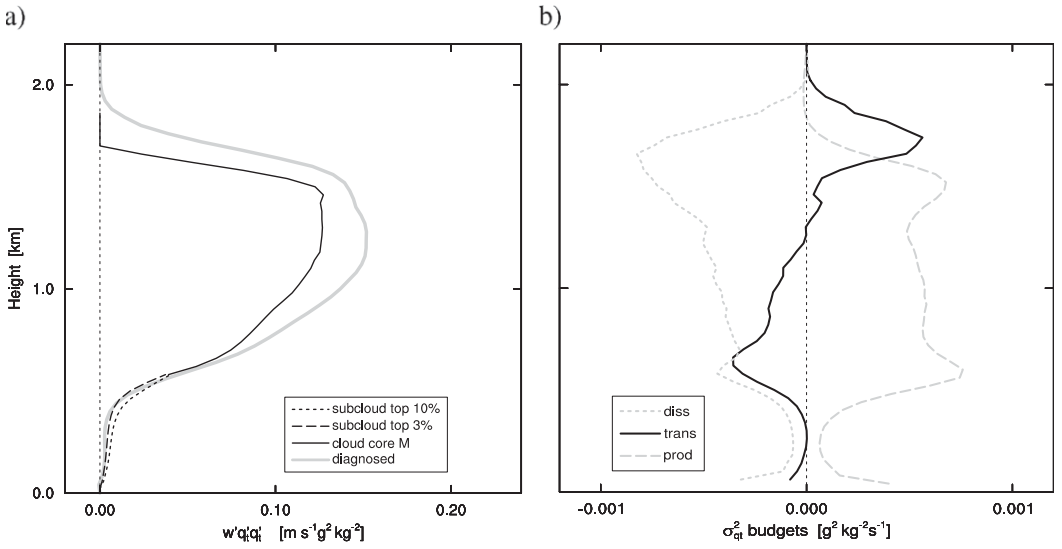

FIG. 3. Aspects of the variance budget for the BOMEX case, using hourly averaged LES profiles. (a) The variance flux $\overline{w'q_l'q_t'}$, both diagnosed (gray) and parameterized by the mass flux approach (black). Shown are the cloud core (black solid) and two top percentages of the PDF of vertical velocity in the subcloud layer (black dashed and dotted, respectively). (b) The LES variance budget. The dissipation term is calculated as a residual of the other terms, assuming steady state.

a larger excess; when substituted in the system (17) and (18), this gives exactly the same variance.

Figure 4b shows an offline evaluation of (17) and (18) for LES in BOMEX. The parameterization reproduces the increasing updraft variance with height in the cloud layer. The small-scale irregularities are caused by the use of an instantaneous snapshot 3D field. The more structural differences between the profiles are probably

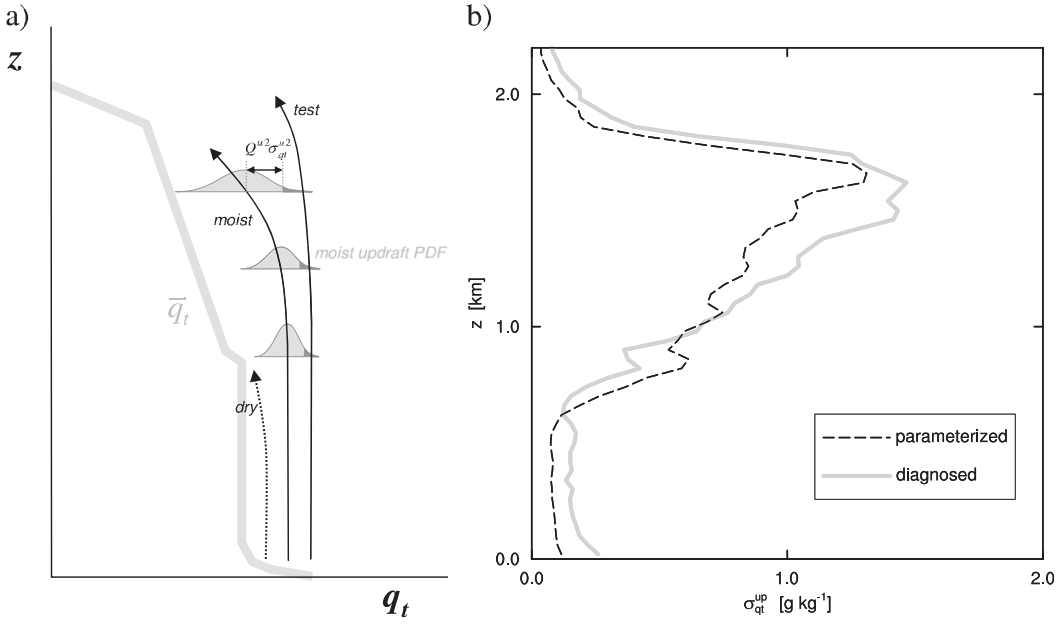

FIG. 4. (a) Schematic illustration of the increasing width of the moist updraft PDF with height as implied by the divergence of single parcel profiles, through closure (17). The test parcel fraction is shaded dark gray. The distance between the lower boundary of the latter and the mean of the updraft PDF ($Q^{u2}\sigma^{u2}_{q_t}$) is indicated by the horizontal arrow. (b) Offline evaluation in LES of parameterization (17) for the variance among moist updrafts σ^{u2}_{qt}, during the BOMEX case.

explained by small departures of the real distribution from a pure Gaussian shape (for example, featuring a nonzero skewness). Nevertheless, the parameterization manages to reproduce the bulk of the magnitude of variance among updrafts and vertical structure.

This technique can be summarized as tying an assumed PDF to a few resolved updrafts to fill in the empty spaces between them. Its evaluation in Fig. 4b suggests that resolving only a few updrafts is already sufficient to recreate the convective variance structure. This could in theory work as well as resolving many more updrafts to render the PDF. Keeping the number of resolved updrafts as low as possible fits the aim in parameterization of searching for the minimum number of free model variables required to represent the impact of unresolved phenomena.

The variance to be used in the statistical cloud scheme has now become closely tied to the updraft model. For a realistic reproduction of convective cloud fraction and condensate, it is a prerequisite that the model updrafts reproduce the divergence as observed in Fig. 4b. As described in Part I of this study, this capability is introduced by the flexible entrainment rate parameterization, featuring an inverse dependence on vertical velocity. This positive feedback mechanism acts to increase spread among updrafts by enhancing sensitivity to initial conditions and updraft environment. This will be evaluated in section 3 using single-column model (SCM) simulations.

d. Offline evaluation using LES

To give proof of principle of the proposed method before the full SCM evaluation, an ''offline'' evaluation of the double PDF framework using LES is now performed for the BOMEX case (see Fig. 5). All required model variables ($\bar{\phi}$, ϕ_{u0}, ϕ_{u2}, a_{u2}, and σ_ϕ) have first been diagnosed in an instantaneous 3D LES field, after which the system of equations is solved. The results show that given the correct background state, the double PDF framework is capable of reproducing the vertical structure and magnitude of both cloud fraction and condensate. The typical peak in cloud fraction at cumulus cloud base is mainly carried by the diffusive PDF G^K, representing forced cumuli. In contrast, in the top half of the cloud layer all cloudiness and condensate is contributed by the updraft PDF G^{up} because of its residence in the saturated part of the $\{\theta_l, q_t\}$ frame (see also Fig. 1b). This structure of the cloud layer is consistent with observed population statistics of shallow cumulus, with many weak updrafts stopping near cloud base and few stronger updrafts managing to rise further.

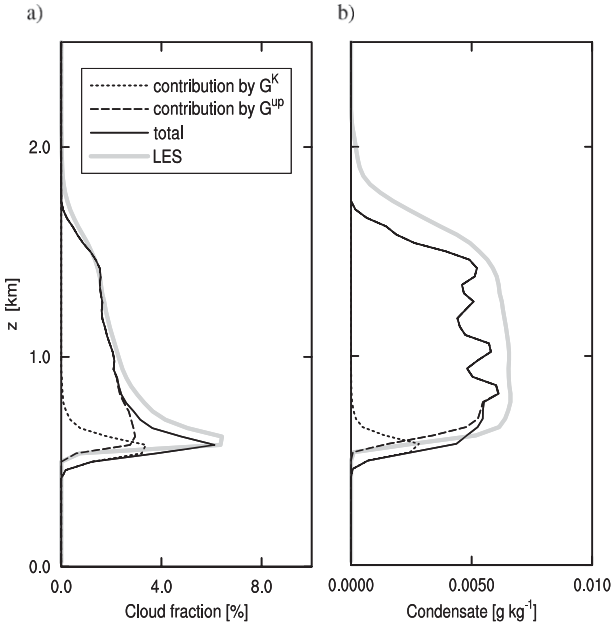

FIG. 5. Offline evaluation of the double PDF cloud scheme using LES for the BOMEX case, featuring (a) total cloud fraction $\mathcal{A}_c$ and (b) total condensate $\bar{l}$. Individual contributions by the updraft PDF and the diffusive PDF are also shown.

e. Precipitation

Finally, the EDMF decomposition is also extended into the representation of precipitation, in the sense that within the PBL each EDMF component precipitates separately; the large-scale precipitation scheme acts on the condensate associated with the diffusive PDF, whereas a convective precipitation scheme acts on the condensate associated with the updraft PDF. PBL precipitation in the DualM scheme thus features two independent modes (or moments), each representing one independent component of the EDMF framework. This makes the treatment of precipitation internally consistent with that of transport and clouds. This is illustrated schematically in Fig. 6.

Use is made of an existing model for updraft precipitation generation and evaporation. Similar to the IFS convection scheme, the PBL updrafts precipitate using the Kessler (1969)–Sundqvist (1978) relations (see the IFS CY31R1 documentation, especially ''Part IV: Physical processes'', available online at http://www.ecmwf.int/research/ifsdocs/). However, the main difference is that the DualM scheme features more than one updraft. A full description of a multiple updraft precipitation scheme is given in appendix D. Shortly summarized, each updraft can precipitate individually, generating its own precipitation flux. This flux consists of two separate shafts for rain and snow. The precipitation generation term in

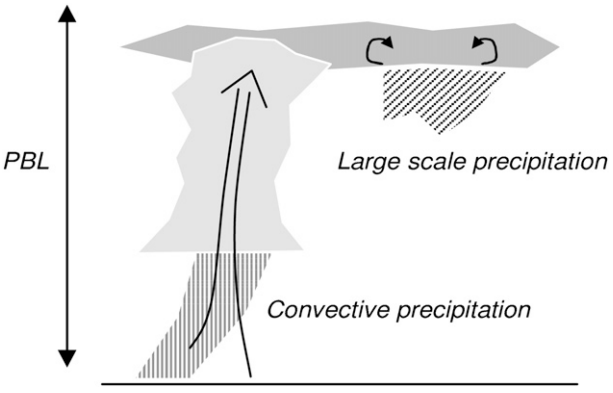

FIG. 6. Schematic illustration of the internally consistent treatment of PBL transport, clouds, and precipitation in the EDMF framework for a scenario featuring cumulus rising into stratocumulus. Light gray represents updraft clouds; dark gray represents passive clouds. The big arrow indicates updraft advective transport; the small circular arrows indicate smaller-scale diffusive transport. The patterned shadings indicate precipitation.

the updraft budget equations affects updraft condensate, which is dependent on a critical updraft condensate value above which precipitation generation becomes efficient.

An important consequence of the introduction of the double PDF cloud scheme is that the condensate associated with the updraft PDF contributes directly to grid box mean condensate. This updraft PDF is reconstructed using updraft profiles, calculated using budget equations in which updraft precipitation is already represented. As a result, after the PBL scheme is called, the updraft part of grid box condensate has already precipitated. This leaves only the diffusive part of the grid box condensate to be treated by the large-scale precipitation scheme, which is called afterward. This situation provides a practical motivation for extending EDMF into precipitation.

3. SCM evaluation

a. Setup

To evaluate the EDMF–DualM scheme—including the new double PDF cloud scheme—it is implemented into the ECMWF IFS, as described in Part I. Within the PBL the new cloud scheme replaces the IFS prognostic cloud scheme (Tiedtke 1993); above PBL top (i.e., the top level of the transporting updraft) the latter is still applied. This configuration completely conserves condensate mass across the PBL boundary. For example, cloud fraction and condensate in the residual PBL is picked up and treated by the prognostic Tiedtke scheme, and vice versa.

Single-column model evaluation is performed for five marine subtropical trade wind scenarios, as developed by the Global Energy and Water Experiment (GEWEX) Cloud System Studies (GCSS; Browning 1993) Boundary Layer Cloud Working Group. A complete summary of acronyms and references is given in Table 1. These cases cover the major cloud structure regimes that occur in the subtropical marine trade wind flow: single-layer stratocumulus, cumulus rising into stratocumulus, and fair-weather cumulus (e.g., Albrecht et al. 1995). The BOMEX case represents shallow cumulus with a relatively small cloud fraction; the Rain in Cumulus over the Ocean (RICO) experiment represents somewhat deeper shallow cumulus. The second Dynamics and Chemistry of Marine Stratocumulus field study (DYCOMS2) represents stratocumulus with strong subsidence, and the Atlantic Trade Wind Experiment (ATEX) represents the transitional regime, featuring cumuli rising into a capping stratocumulus layer under a strong inversion. Finally, a subtropical Lagrangian scenario is evaluated [a variation on the GCSS Atlantic Stratocumulus Transition Experiment (ASTEX) case], during which a complete transition takes place from stratocumulus to fair-weather cumulus.

LES results are obtained using code from the Royal Netherlands Meteorological Institute (KNMI) and from the GCSS Data Integration for Model Evaluation (DIME) archive. All SCM simulations are performed at the L91 vertical resolution of IFS, featuring 91 atmospheric levels of which 17 are located in the lowest 2 km (see Table A1 in appendix A). For the marine equilibrium scenarios, the period of simulation is always 4 days to allow the model to equilibrate.

b. Marine equilibria

Figures 7–9 show the mean and cloudy state as reproduced by the SCM including the double PDF cloud scheme. In general, the vertical structure of PBL mean specific humidity, cloud fraction, and cloud condensate is reproduced for all cases. For the BOMEX case, the results of the offline evaluation using LES (see also Fig. 5) carry over to the full SCM simulation, featuring the typical decreasing cloud fraction profile with height and the more or less constant condensate in the cloud layer. For the ATEX case, the typical double-peak profile characteristic of cumulus rising into stratocumulus is reproduced. For the DYCOMS2 case, a total cloud cover of 100% is reproduced (unfortunately no LES data on DYCOMS2 cloud fraction were available to the authors), as well as the relatively high total condensate values typical for this subsidence regime.

The results illustrate that the diffusive PDF acts to represent passive and stratiform clouds, whereas the updraft PDF represents cumuliform clouds. The diffusive PDF acts to increase cloud fraction and condensate

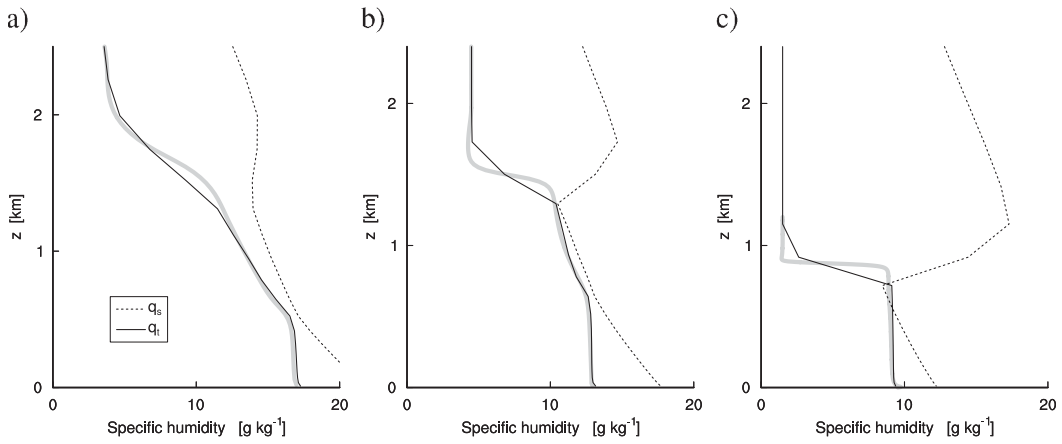

FIG. 7. SCM results of the DualM scheme featuring the double PDF cloud scheme, showing mean total specific humidity q_t (solid) and q_{sat} (dotted) for the (a) BOMEX, (b) ATEX, and (c) DYCOMS2 case. LES results are plotted in thick gray. The SCM results reflect 24-h averages.

automatically when the mean state approaches saturation—for example, at shallow cumulus cloud base or near the capping inversion if the latter is strong enough. As explored in Part I, the proximity of mixed layer top to the saturation curve is caused by (i) the closure of the moist updraft area fraction, requiring condensation of updrafts, and (ii) transport by the dry updraft, which continuously detrains specific humidity in the cloud base transition layer. This detrainment flux also contributes to the variance of the diffusive PDF through the production flux in (12). The result is a peak in cloud fraction at cloud base, a characteristic feature of shallow cumulus convection.

The role of the updraft PDF is to create enough cloud fraction and condensate in conditionally unstable cloud layers (see Figs. 8a and 9a). In those situations the mean state in the cloud layer can be relatively far from the saturation curve (low relative humidity), and the updraft PDF then forms an isolated mode in the saturated section of conserved variable space. This is the situation visualized schematically in Fig. 1b. Another role of the updraft PDF is to create cloudiness and condensate associated with updrafts overshooting a capping stratus layer (visible in the ATEX case).

The scenario that best demonstrates the benefits of an advective–diffusive decomposition in subgrid cloud representation (and the associated close coupling between the transport and cloud schemes) is the transitional ATEX case. Because of the entrainment efficiency closure at PBL top and the feedback of stability on the vertical structure of cloudy mass flux, the transport model acts to increase humidity flux convergence under stronger inversions, as testified by the steeper $\overline{q_t}$ profile shown in Fig. 7b. The resulting high local relative humidity then helps the formation and maintenance of

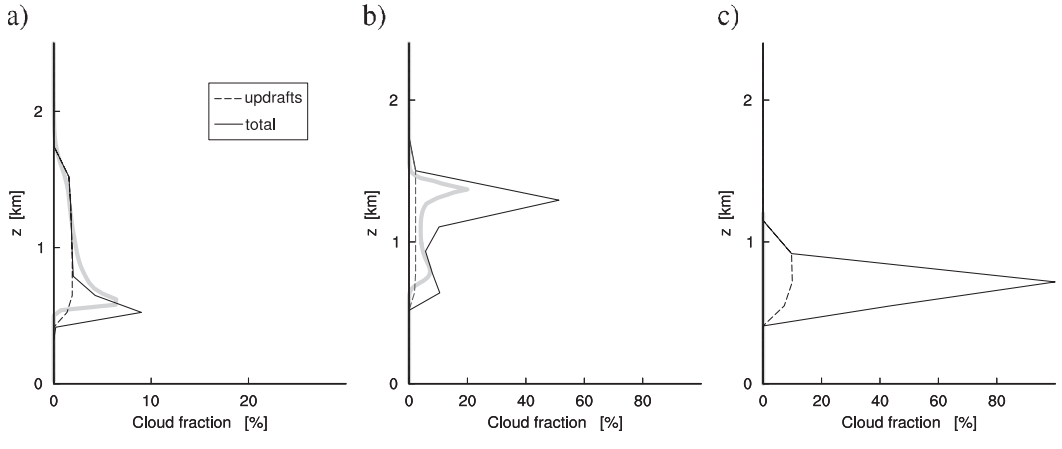

FIG. 8. As in Fig. 7, but for total cloud fraction $\mathcal{A}_c$. The individual contribution by the updraft PDF is plotted as a dashed line. Note that the plotting range in (a) is different to aid visualization.

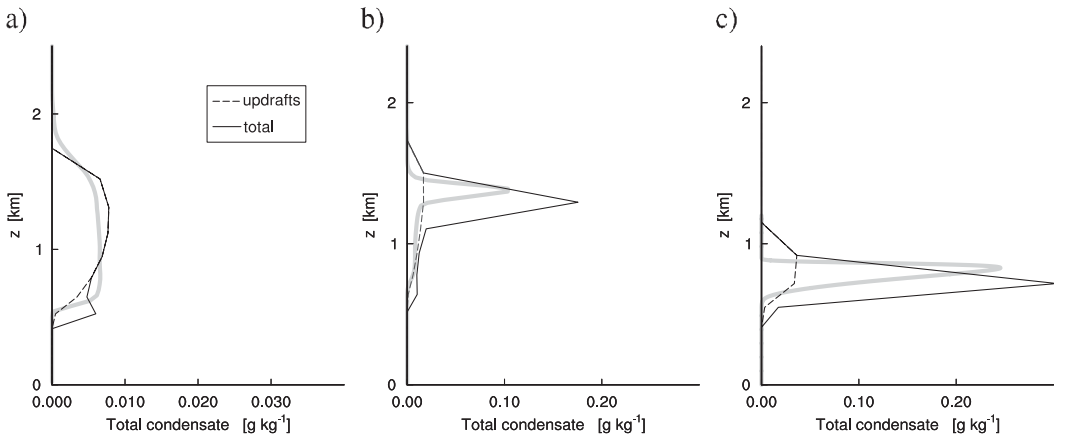

FIG. 9. As in Fig. 8, but for total condensate $\bar{l}$.

the capping stratocumulus layer through the diffusive PDF. In turn, the updraft component of EDMF contributes most of the cloud fraction and condensate at lower heights, representing the cumuli that are rising into the stratocumulus layer.

The double PDF of q_t as reproduced for the BOMEX case is evaluated against LES results in Fig. 10. The PDFs at three heights in the cloud layer are shown. In LES most air has properties close to the grid box mean, a feature that is represented in the model through the large fraction of air that is assigned to the diffusive PDF. On the other hand, only little air shows large positive excesses, represented in the model by the small fraction of air assigned to the updraft PDF. In general the changing shape of the distribution with height is reproduced: (i) the decreasing width of the main PDF, (ii) the increasing separation of the strongest updrafts from the mean state, and (iii) the stretching of the updraft tail. In the SCM these features are represented by, respectively, (i) the decreasing width of the diffusive PDF, (ii) the increasing excesses of the updraft PDF mean, and (iii) the increasing width of the updraft PDF.

The variance structure as produced by the DualM scheme is evaluated in Figs. 11 and 12 for the BOMEX and DYCOMS2 cases. Figure 11a shows that the first-order vertical structure and magnitude of the individual terms in the variance budget are reproduced. Variance production peaks at mixed layer top and near the inversion (although somewhat underestimated), while transport removes variance from mixed layer top and deposits it near cloud top. At that height the transport term is as important as the production term; note that the transport maximum is located just above the production maximum, a characteristic feature in LES that is reproduced by the SCM. In contrast, in the DYCOMS2 stratocumulus case variance transport plays a less important role.

The EDMF decomposition of variance is shown in Fig. 12. In this figure the contribution to the total variance by the updraft area is shown, which relates to the variance among updrafts $\sigma_\phi^{\mathrm{up2}}$ that appears in (11) as

$$\overline{q_t'^2}^{\mathrm{up}} = \sigma_\phi^{\mathrm{up2}} + (\bar{\phi} - \overline{\phi}^{\mathrm{up}})^2, \tag{19}$$

where the prime indicates a perturbation from the grid box mean. In the cumulus cloud layer (see Fig. 12a) the updraft contribution to variance becomes dominant near cloud top, reflecting the large excesses of this small fraction of air over the environment. In contrast, the updraft contribution is negligible in the stratocumulus case (see Fig. 12b) because of the much smaller excesses of the updrafts. The large variance peak below PBL top as seen in LES is associated with the strong but shallow inversion layer; at the much coarser resolution in the SCM this cannot be resolved. Instead, the variance is smaller but covers a thicker (model) layer.

The precipitation model is evaluated in Fig. 13. Large-scale precipitation acts on the condensate associated with the diffusive PDF. As a result, it becomes less and less important relative to convective precipitation when moving downstream along the trade wind trajectory because of the disappearing passive stratus clouds. For example, near cloud top in the DYCOMS2 case the updraft and large-scale contributions to the total precipitation are roughly equal. In the ATEX case the capping stratus layer still precipitates significantly, but the convective contribution is already much larger. In the BOMEX case, the small contribution to cloud fraction and condensate by the diffusive PDF at cloud base (see Figs. 8a and 9a) does produce some large-scale precipitation but is obscured by the convective flux. The BOMEX case has its maximum precipitation flux in the

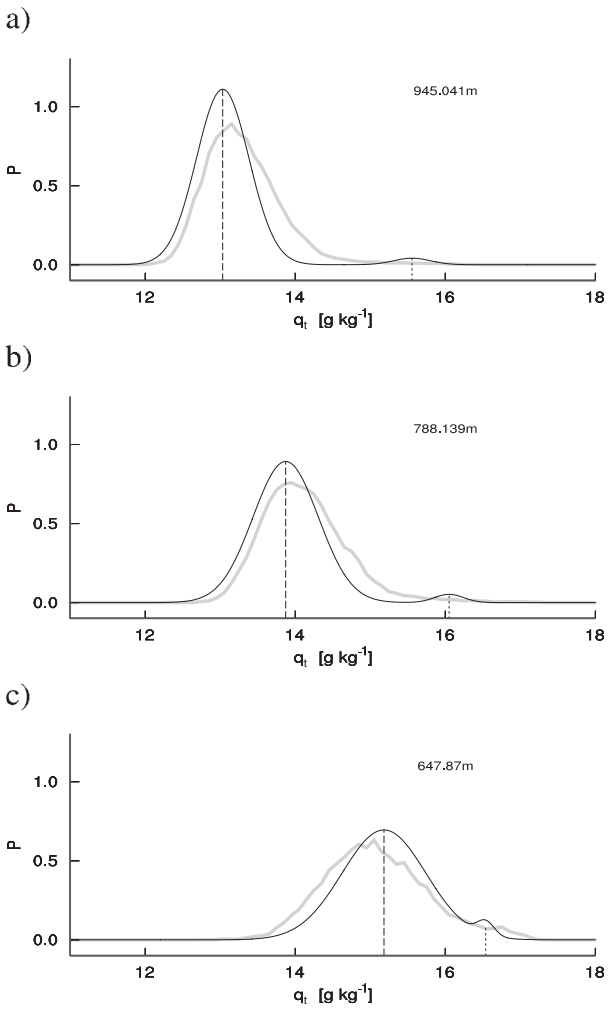

FIG. 10. Evaluation of the double PDF of q_t as produced by the SCM (solid black) against LES (gray) at various heights in the BOMEX cloud layer. The dotted line indicates the mean of the updraft PDF; the dashed line indicates the mean of the diffusive PDF. The LES distributions are obtained from a single instantaneous 3D LES field.

middle of the cloud layer, corresponding to the level where precipitation generation equals evaporation. Below this level evaporation dominates, as a result of which the precipitation flux has decreased substantially when it reaches the surface. This behavior is shared by most of the LES codes that participate in the GCSS intercomparison on the RICO shallow cumulus case.

A benefit of applying the EDMF partitioning to both clouds and precipitation is apparent in the DYCOMS2 case; although the diffusive contribution to condensate clearly dominates over the updraft contribution (see Fig. 9c), their precipitation fluxes have almost the same magnitude (see Fig. 13c). This can be explained by the fact that moist cumulus updrafts have relatively high condensate values but occupy a relatively small area. Although the precipitation generation model is an exponential function of updraft condensate, the subsequent weighting by the moist updraft area fraction is linear (see appendix D). Apparently, in this case, this makes the net contribution by updrafts to the total precipitation still relatively important.

Finally, the impact of updraft precipitation on the structure of cloud layer condensate is evaluated in Fig. 14 for the RICO case. Because in this scheme updraft profiles are used to reconstruct the updraft PDF that is part of the double PDF cloud scheme, the precipitation term in the updraft budget directly affects grid box mean condensate. This should become apparent in deeper shallow cumulus regimes such as RICO in which precipitation starts to play a significant role. Figure 14a shows that this is indeed the case, illustrating the strong fingerprint of updraft condensate structure on the total condensate. It also indicates that in this case updraft precipitation is required to obtain realistic magnitude and vertical structure of mean condensate in the top half of the cloud layer.

c. A stratocumulus to cumulus transition

We now progress to a more challenging scenario that describes a complete transition in trade wind cloud structure, from stratocumulus to fair-weather cumulus. All the different cloud regimes studied in the previous section occur during this transition. It is educational to assess whether, and if so why, the model can represent gradual changes between the various cloud regimes. The scenario studied here is the ''Dbase'' case as formulated by Wyant et al. (1997). A main difference with the GCSS ASTEX Lagrangian case is that the prescribed large-scale divergence is kept constant in time. As a result, the cloud transition will be solely driven by the prescribed, linearly increasing SST. This simplified setup enhances the transparency of the case, which should facilitate the analysis of model physics. The solar insulation follows a diurnal cycle, which will also impact the cloud properties.

Figure 15a shows that a gradual transition in cloud structure is reproduced by the DualM scheme. The first 5 days feature a low stratocumulus layer with total sky cover (see Fig. 15c). As time progresses the cloud top rises gradually. After day 7, a second, small maximum in cloud fraction starts to emerge below the capping stratocumulus cloud layer, coinciding with the lifting condensation level (LCL) of the moist updraft. This situation represents cumulus rising into stratocumulus. Simultaneously, cumulus overshoots start to appear above the capping cloud layer, the latter now weakening and

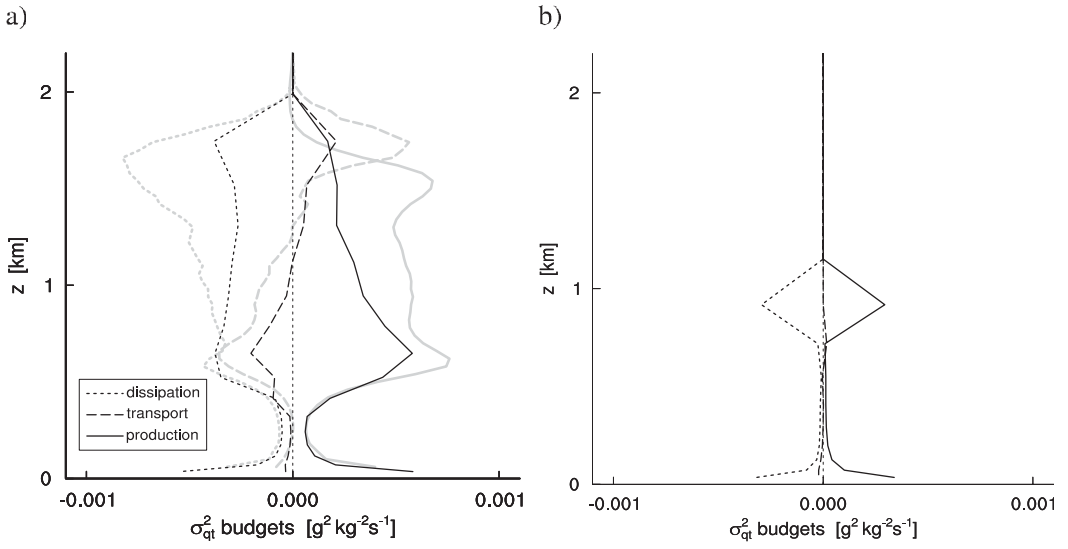

FIG. 11. Variance budgets for (a) BOMEX and (b) DYCOMS2 as reproduced by the DualM scheme. The corresponding LES sampled budgets (only available for the BOMEX case) are shown in gray.

breaking up. This cloud layer could now also be referred to as a ''cumulus outflow layer''. Finally, at day 9, the capping cloud layer has disappeared, indicating fair-weather cumulus. The vertical profiles of cloud fraction shown in Fig. 15b further illustrate that the three major cloud regimes do occur in the simulation.

Perhaps the most important result is that a smooth transition in cloud structure is reproduced. A key feature is the gradual emergence of updraft LCL below stratocumulus cloud base (as indicated in Fig. 15a by the dotted line). Whereas updraft LCL height is tightly controlled by the updraft initial excesses of temperature and humidity, the capping cloud layer is attached to and controlled by the inversion through the stability-dependent top entrainment. As a result, the updraft LCL and stratocumulus cloud base can evolve independently and differently in the model. When entrainment efficiency increases (because of the weakening inversion), the capping cloud layer thins, accompanied by a rise in its cloud base height. As a result, at some point in the simulation ($t \approx 7$ days) updraft LCL drops below cloud base of the capping cloud layer—a situation that corresponds to cumulus rising into stratocumulus. The moist convective inhibition closure, represented

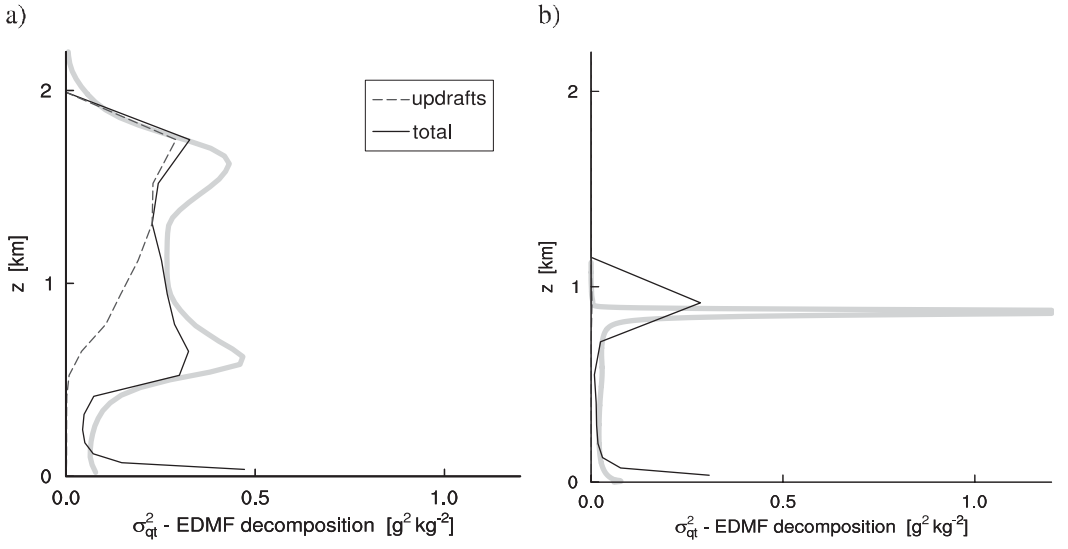

FIG. 12. As in Fig. 11, but for the EDMF decomposition of variance as reproduced by the DualM scheme.

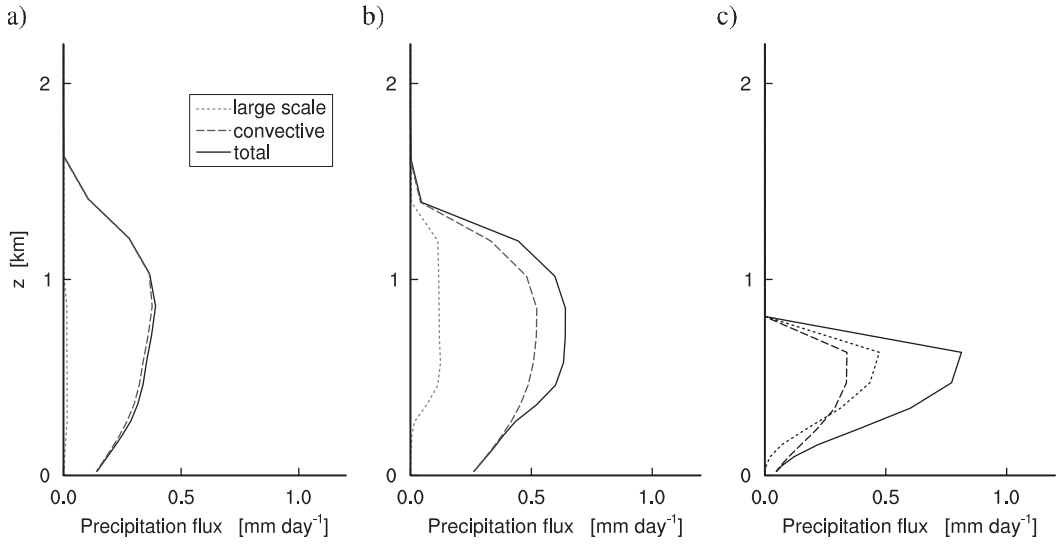

FIG. 13. The precipitation flux for (a) BOMEX, (b) ATEX, and (c) DYCOMS2 as reproduced by the DualM scheme, showing the individual contributions by updraft (dashed) and large-scale (dotted) precipitation.

through the moist updraft area fraction, then acts to keep the mean state close to saturation near mixed layer top (updraft LCL), causing the formation of the characteristic second maximum in cloud fraction at that height.

d. Sensitivity to model constants

The model evaluation is concluded by an assessment of the sensitivity of model outcome to constants of proportionality. Preliminary SCM tests with the scheme

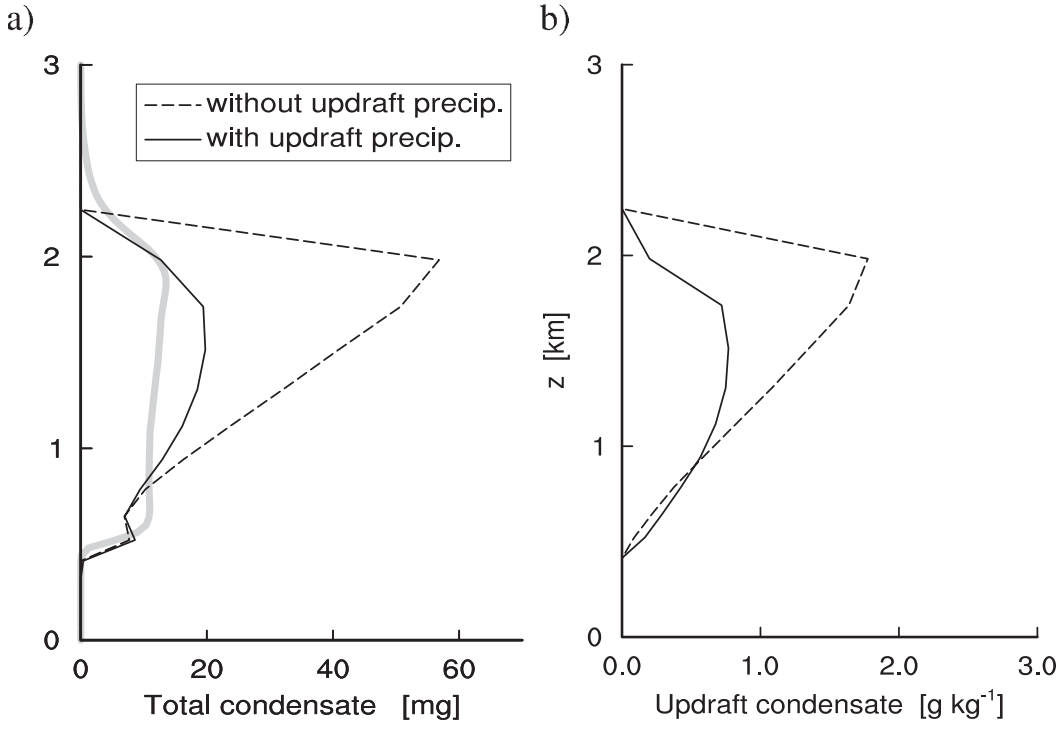

FIG. 14. Impacts of updraft precipitation on cloud layer structure during the RICO case, showing (a) the total condensate and (b) the moist updraft condensate of two SCM experiments, one with (solid) and one without (dashed) updraft precipitation. The SCM lines represent instantaneous profiles at $t = 1$ day, for visualization of the fingerprint of updraft condensate structure on the total condensate. LES results are shown in thick gray.

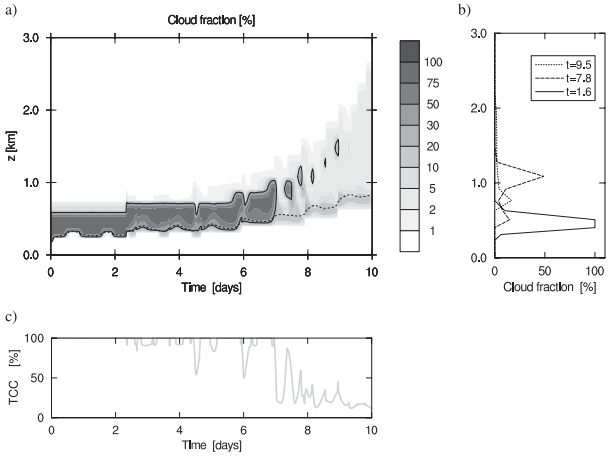

FIG. 15. DualM results for the stratocumulus to cumulus transition case. (a) Time–height contour plot of cloud fraction. Small values are emphasized to allow visualization of cumulus cloud fraction. The 30% contour line is plotted in black to highlight the capping cloud layer. The dashed line indicates lifting condensation level of the moist updraft. The simulations start at midnight local time. (b) Vertical profiles of cloud fraction at three selected moments in the simulation. (c) The associated time series of total cloud cover (TCC).

revealed that two model constants carry the greatest sensitivity: (i) the variance dissipation time scale τ_σ and (ii) the critical condensate q_l^{crit} in the updraft precipitation generation model (D1). These can best be demonstrated for the RICO case because significant precipitation occurs in this scenario.

Figure 16a illustrates the sensitivity of the cloud fraction profile to the variance dissipation time scale τ_σ. As illustrated earlier, the typical ''foot'' in the cumulus cloud fraction profile is carried by the diffusive PDF. A larger dissipation time scale leads to a larger variance. As a result, at cloud base where relative humidity is high, a wider diffusive PDF then easily leads to a larger saturated fraction. The updraft contribution to cloud fraction remains unaffected; this is due to the independent parameterization of the updraft PDF purely as a function of updraft properties.

Figure 16 documents that a large sensitivity exists in the representation of clouds to the critical condensate q_l^{crit} in the Kessler–Sundqvist precipitation generation model. This is particularly evident in (i) the total condensate, (ii) the surface precipitation rate, and (iii) the cloud top height (which reduces for more intense rain). The total condensate almost doubles over the explored range; an impact of the same order of magnitude can be expected in the radiative response. The surface precipitation almost triples over the explored range. This is worrying because this parameter is such an important parameter in the atmosphere's energy budget. More studies of observational or high-resolution numerical datasets are required to either (i) constrain this important parameter often used in 1D models or (ii) discard this precipitation generation model completely if it proves to be flawed.

4. Concluding remarks

In this study the EDMF framework is used to integrate the representation of subgrid diffusive transport, advective transport, and clouds in the PBL. This is achieved by parameterizing all processes in terms of the

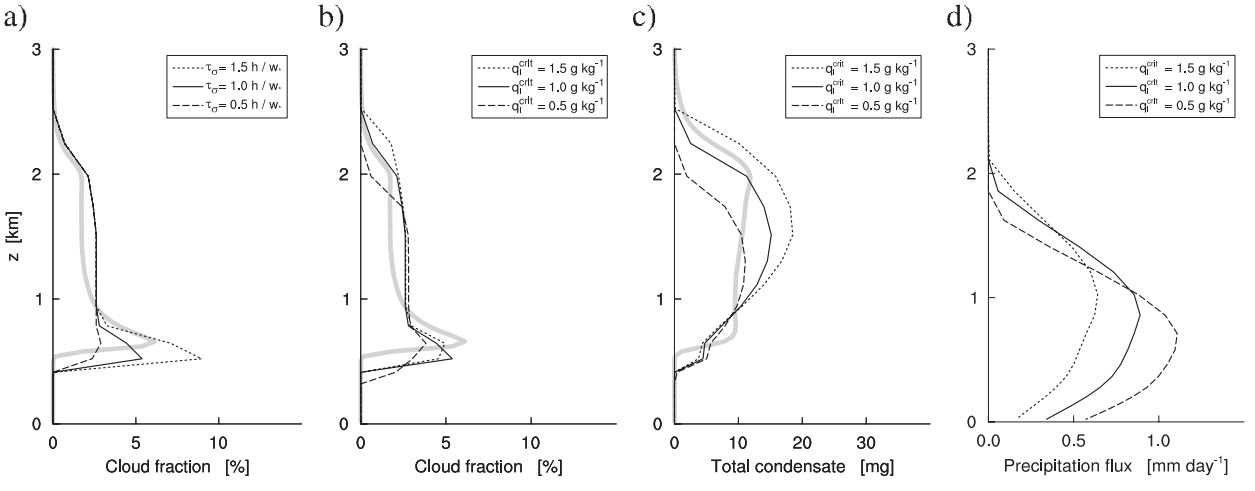

FIG. 16. Sensitivity of RICO results to two important model constants: (a) cloud fraction as a function of τ_σ, (b) cloud fraction as a function of q_l^{crit}, (c) condensate as a function of q_l^{crit}, and (d) precipitation flux as a function of q_l^{crit}. The profiles reflect time averages over the first day of simulation to allow visualization of the differences in PBL deepening rate in the sensitivity test on q_l^{crit}. LES profiles are plotted in gray.

same reconstructed turbulent distribution, making their representation internally consistent throughout the PBL. Including an additional PDF enhances model complexity, which allows representation of more complex scenarios. The evaluation for a series of prototype scenarios demonstrates that this technique is successful in reproducing the cloudy structure of the major convective PBL regimes, as well as transitions between those.

An integrated representation of boundary layer clouds and transport, made possible by their unique (turbulent) nature, has some useful consequences. First, successfully reproducing one process requires accurate representation of the other. This means that PBL scheme development always involves the whole set of physics and not just one individual part. Second, a reduction in the number of separate model components reduces the opportunities for tuning model constants, thus limiting the chance that compensating errors can occur. Third, the results show that the enhancement in model complexity that was required for unification does not necessarily lead to model instability, and it also allows for representation of more complex scenarios, such as the transitional trade wind regime.

The applicability of an advective–diffusive decomposition to both cloudiness and transport in the convective boundary layer forms the foundation of this integrated modeling approach. In principle, the EDMF approach can be applied to any process that features the same advection–diffusion bimodality. For example, Kuang and Bretherton (2006) show that bimodal PDFs also exist in deep convective situations, with rising convective towers and capping cirrus outflow layers at the tropopause. Another example is mixed-phase stratocumulus, such as that observed during the Mixed-Phase Arctic Clouds Experiment (M-PACE; Harrington and Verlinde 2004; Verlinde et al. 2005), in which updraft condensate is often found to be mainly in liquid phase while the stratus layer contains most of the ice. However, the representation of mixed-phase cloud microphysics probably requires more model complexity than is contained in the current scheme.

The EDMF–DualM framework, as presented in this study, was developed for use in the ECMWF IFS. The impacts on the 3D model global climate and medium-range forecasts will be presented in a forthcoming ECMWF ARM report, currently in preparation. Among others, beneficial changes in global model climate are reported, such as the spatial distribution of low-level subtropical marine clouds, the associated shortwave radiative cloud forcing, and the representation of summertime low-level shallow cumulus at the ARM SGP site. The sensitivity of model cloud–radiative climate to various DualM components will be assessed.

Acknowledgments. While affiliated at ECMWF, the author was sponsored by the Atmospheric Radiation Measurement (ARM) Program of the United States Department of Energy (DOE). LES results for the DYCOMS2 RF01 case were obtained from the GCSS Data Integration for Model Evaluation (DIME) archive. Margreet van Zanten is thanked for kindly providing the KNMI LES data for the GCSS RICO case. We thank Philippe Bougeault for critically reading this manuscript and for his knowledgeable feedback on the statistical cloud model and various other members of staff at ECMWF for their generous support. We finally thank Bjorn Stevens and three anonymous reviewers for their constructive comments on this study.

APPENDIX A

Precalculated Functions

Table 2 contains a range of values of the Gaussian shape functions $\mathcal{B}$ and $\mathcal{D}$ as a function of the normalized deficit Q; $\mathcal{B}$ represents the fraction of a top segment of the normal distribution as defined by Q and $\mathcal{D}$ represents its mean. The values are calculated using the normal probability function,

$$P(x) = \frac{1}{\sigma_x\sqrt{2\pi}} e^{\left[-\frac{1}{2}\left(\frac{x-\bar{x}}{\sigma_x}\right)^2\right]} \tag{A1}$$

with $\bar{x} = 0$ and $\sigma_x = 1$. In the PBL scheme, interpolation is used to estimate the in-between values.

Table A1 gives the heights of the lower boundaries of the lowest 21 model layers of the IFS L91 vertical discretization, calculated using initial RICO case atmospheric conditions.

APPENDIX B

Linearization of q_{sat}

Figure 2 suggests that the variation of q_{sat} in convective cloud layers is significant. This is explained by the dependence of q_{sat} on temperature, the latter featuring considerable variation in the cloudy tail of the turbulent PDF as a result of varying updraft mixing rates and differential latent heat release (Sommeria and Deardorff 1977). We assumed earlier that the joint PDF lies on a linear axis,

TABLE A1. The height of the lower boundary of the lowest 21 model layers of the IFS L91 vertical discretization. The heights are approximate, calculated using the initial atmospheric conditions of the RICO case (1015.4 Pa surface pressure, T = 299.2 K at the surface).

Level	Height (m)	Level	Height (m)	Level	Height (m)
71	2974	78	1205	85	277
72	2666	79	1024	86	205
73	2377	80	859	87	142
74	2107	81	711	88	90
75	1855	82	579	89	50
76	1621	83	463	90	21
77	1404	84	363	91	0

$$q_t(x) = q_t(x_{\text{sat}}) + \frac{\partial q_t}{\partial x}|_{x_{\text{sat}}}(x - x_{\text{sat}}), \tag{B1}$$

where x_{sat} is the intersection point of the axis and the saturation curve. In combination with the usual local Taylor expansion of the saturation curve, this implies that q_{sat} (x) can be linearized around x_{sat} as well:

$$q_{\text{sat}}(x) = q_t(x_{\text{sat}}) + \frac{\partial q_{\text{sat}}}{\partial x}|_{x_{\text{sat}}}(x - x_{\text{sat}}). \tag{B2}$$

This allows writing the total condensate at some point x in the cloudy part of the PDF as

$$q_t - q_{\text{sat}} = C(x - x_{\text{sat}}), \tag{B3}$$

where

$$C = \left(\frac{\partial q_t}{\partial x} - \frac{\partial q_{\text{sat}}}{\partial x}\right)_{x_{\text{sat}}} \tag{B4}$$

is a factor always larger than zero because the presence of condensate implies that $q_t > q_{\text{sat}}$. As oversaturation increases linearly beyond x_{sat}, the integral giving PDF-mean condensate l can then be simplified as

$$\begin{aligned} l &= \int_{x_{\text{sat}}}^{\infty} (qt - q_{\text{sat}})P(x)dx, \\ &= C\int_{x_{\text{sat}}}^{\infty} (x - x_{\text{sat}})P(x)dx, \\ &= f\,C\,(\bar{x}^f - x_{\text{sat}}), \end{aligned} \tag{B5}$$

where $P(x)$ is the normal probability function (A1).

APPENDIX C

Saturation Deficit in Conserved Variable Space

The intersection point S_{min} of a linearized PDF axis and the dry saturation curve is obtained using vector calculus (see Fig. C1). We now formulate this method using the updraft PDF as an example (but the principle could apply to any PDF). The axis is defined by the mean state point $\overline{\mathbf{\Phi}}$ and the moist updraft point $\mathbf{\Phi}_{u2}$,

$$\overline{\mathbf{\Phi}} = (\bar{\theta}_l, \bar{q}_t, 0) \quad \text{and} \tag{C1}$$

$$\mathbf{\Phi}_{u2} = (\theta_{l,u2}, q_{t,u2}, 0), \tag{C2}$$

where the third dimension corresponds to the axis perpendicular to the θ_l, q_t plane. The dry saturation curve is linearized as usual, spanned between $\overline{\mathbf{S}}$ and $\mathbf{S}_{u2}$, defined as

$$\overline{\mathbf{S}} = (\bar{\theta}_l, q_{\text{sat}}|_{T=\bar{T}_l}, 0) \quad \text{and} \tag{C3}$$

$$\mathbf{S}_{u2} = (\theta_{l,u2}, q_{\text{sat}}|_{T=T_{l,u2}}, 0), \tag{C4}$$

where T is temperature and $T_l \equiv \theta_t\Pi$ is liquid water temperature. A new system is then defined by the following three orthogonal basis vectors:

$$\hat{\mathbf{n}}_s^{\parallel} = \frac{\mathbf{S}_{u2} - \overline{\mathbf{S}}}{\| \mathbf{S}_{u2} - \overline{\mathbf{S}} \|}, \tag{C5}$$

$$\hat{\mathbf{n}}_s^{\odot} = (0, 0, 1), \quad \text{and} \tag{C6}$$

$$\hat{\mathbf{n}}_s^{\perp} = \hat{\mathbf{n}}_s^{\parallel} \times \hat{\mathbf{n}}_s^{\odot}. \tag{C7}$$

The linear mixing line is vectorized,

$$\mathbf{v} = \mathbf{\Phi}_{u2} - \overline{\mathbf{\Phi}}, \tag{C8}$$

as is the distance of the mean state from the dry saturation curve,

$$\mathbf{d} = \overline{\mathbf{S}} - \bar{\Phi}. \tag{C9}$$

A series of projections is then made onto the new axes $\hat{\mathbf{n}}_{s,}$

$$\upsilon^{\perp} = \frac{\upsilon \cdot \hat{\mathbf{n}}_s^{\perp}}{\| \hat{\mathbf{n}}_s^{\perp} \|}, \quad \upsilon^{\parallel} = \frac{\boldsymbol{\upsilon} \cdot \hat{\mathbf{n}}_s^{\parallel}}{\| \hat{\mathbf{n}}_s^{\parallel} \|}, \quad \text{and} \tag{C10}$$

$$d^{\perp} = \frac{\mathbf{d} \cdot \hat{\mathbf{n}}_s^{\perp}}{\| \hat{\mathbf{n}}_s^{\perp} \|}, \quad d^{\parallel} = \frac{\mathbf{d} \cdot \hat{\mathbf{n}}_s^{\parallel}}{\| \hat{\mathbf{n}}_s^{\parallel} \|}. \tag{C11}$$

This finally allows expressing the intersection point $\mathbf{S}^{\text{min}} = (\theta_l^{\text{min}}, q_{\text{sat}}^{\text{min}}, 0)$ in terms of these projections,

$$\mathbf{S}^{\text{min}} = \overline{\mathbf{S}} + \left(d^{\parallel} + \upsilon^{\parallel}\frac{d^{\perp}}{\upsilon^{\perp}}\right)\hat{\mathbf{n}}_s^{\parallel}. \tag{C12}$$

When $\upsilon^{\perp} = 0$, the PDF is either totally saturated or totally unsaturated, in which case the scheme reverts to an all-or-nothing scheme. Figure 17b illustrates that the linearization of both the PDF axes and the saturation

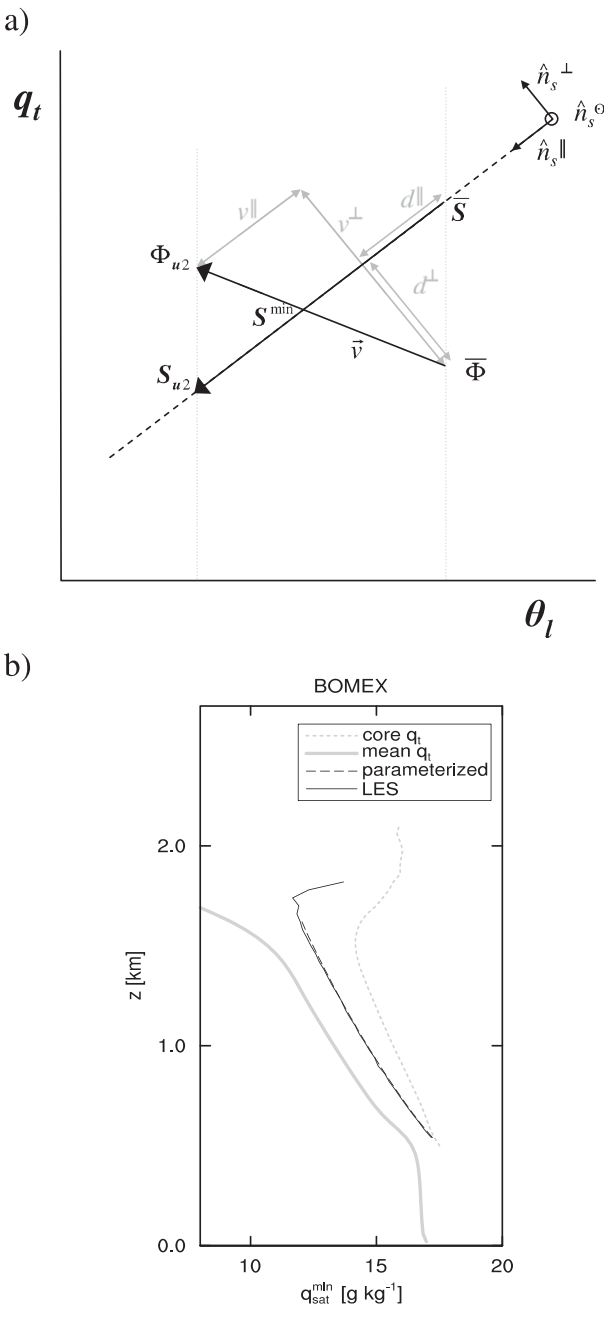

FIG. C1. (a) Visualization of the method for estimating the minimum saturation point $\mathbf{S}^{\min}$ and (b) BOMEX vertical profile of $q_{\text{sat}}^{\min}$, both parameterized (dashed black) and sampled (solid black) in LES. For reference the total specific humidity of the mean state $\overline{q_t}$ (solid gray) and the cloud core q_t^{co} (dotted gray) are also shown.

curve as applied in this method gives reliable estimates of $q_{\text{sat}}^{\min}$ throughout the cloud layer. The last remaining operation is then to use (7) to project $\mathbf{S}^{\min}$ on the PDF axis,

$$x_{\text{sat}} = \frac{(\mathbf{S}^{\min} - \overline{\mathbf{\Phi}}) \cdot \hat{v}}{\| \hat{v} \|}, \tag{C13}$$

for use in the calculation of PDF saturated fraction f and condensate l [see (6) and (8), respectively].

APPENDIX D

Multiple Updraft Precipitation

Each updraft i in the ensemble generates its own precipitation. Following the method of Sundqvist (1978), precipitation generation in updraft i (G_{ui}) acts on updraft total condensate $q_{l,ui}$ and can be written as

$$G_{ui} = c_0 \, q_{l,ui} \left[1 - e^{-\left(\frac{q_{l,ui}}{q_l^{\text{crit}}}\right)^2} \right], \tag{D1}$$

with $c_0 = 1.5 \times 10^{-3}$ s^{-1} representing a characteristic autoconversion inverse time scale and $q_l^{\text{crit}} = 1$g kg^{-1} a critical value of the updraft condensate, above which this process becomes efficient. In the updraft budgets of $\{q_t, \theta_l\}$ as described in Part I, the precipitation generation term r_{ui} acts to dry and warm a cloudy updraft:

$$r_{ui}^{qt} = -G_{ui} \quad \text{and} \tag{D2}$$

$$r_{ui}^{\theta_l} = \frac{\alpha L_v G_{ui} + (1-\alpha) L_s G_{ui}}{c_p \, \Pi}, \tag{D3}$$

with α the fraction of generated precipitation that is in liquid phase. Precipitation generation is then added to the updraft precipitation flux R, maintaining two separate shafts for rain (R_{ui}^r) and snow (R_{ui}^s):

$$R_{ui}^r(p) = \int_0^p (\alpha G_{ui} - \gamma E_{ui} + m_{ui}) \frac{dp'}{g} \quad \text{and} \tag{D4}$$

$$R_{ui}^s(p) = \int_0^p [(1-\alpha) G_{ui} - (1-\gamma) E_{ui} - m_{ui}] \frac{dp'}{g}, \tag{D5}$$

where p is pressure, $R_{ui}^r/(R_{ui}^r + R_{ui}^s)$ is the rain fraction of the updraft precipitation flux at any level, and m_{ui} is the melting tendency of snow into rain. Updraft precipitation evaporation E_{ui} follows the algorithm of Kessler (1969). It acts on the combined updraft rain and snow fluxes and is assumed to take place in the updraft environment,

$$E_{ui} = 5.44 \times 10^{-4} [q_{\text{sat}}(\bar{T}) - \overline{q_v}] \left(\sqrt{\frac{p}{p_0}} \frac{R_{ui}^r + R_{ui}^s}{5.09 \times 10^{-3}} \right)^{0.577}, \tag{D6}$$

with the constants as proposed by Kessler (1969). Finally, multiple updraft precipitation appears in the

mean state budgets of $\{\overline{q_t}, \overline{\theta_t}\}$ as a summated flux divergence term,

$$\frac{\partial \overline{q_t}}{\partial t}|_R = -g\frac{\partial}{\partial p}\sum_{i=1}^{I} a_{ui}(R^r_{ui} + R^s_{ui}) \quad \text{and} \tag{D7}$$

$$\frac{\partial \overline{\theta_l}}{\partial t}|_R = g\frac{\partial}{\partial p}\sum_{i=1}^{I}\frac{a_{ui}(L_v R^r_{ui} + L_s R^s_{ui})}{c_p \Pi}, \tag{D8}$$

in the DualM scheme $I = 2$, featuring a dry and a moist (cloudy) updraft. As a consequence of this choice, only the latter generates precipitation.

REFERENCES

Albrecht, B. A., C. S. Bretherton, D. Johnson, W. Schubert, and A. S. Frisch, 1995: The Atlantic Stratocumulus Transition Experiment (ASTEX). *Bull. Amer. Meteor. Soc.,* **76,** 889–904.

Augstein, E., H. Riehl, F. Ostapoff, and V. Wagner, 1973: Mass and energy transports in an undisturbed Atlantic trade-wind flow. *Mon. Wea. Rev.,* **101,** 101–111.

——, H. Schmidt, and V. Wagner, 1974: The vertical structure of the atmospheric planetary boundary layer in undisturbed trade winds over the Atlantic Ocean. *Bound.-Layer Meteor.,* **6,** 129–150.

Bougeault, P., 1981: Modeling the trade-wind cumulus boundary layer. Part I: Testing the ensemble cloud relations against numerical data. *J. Atmos. Sci.,* **38,** 2414–2428.

Bretherton, C. S., S. K. Krueger, M. C. Wyant, P. Bechtold, E. Meijgaard, B. Stevens, and J. Teixeira, 1999: A GCSS boundary-layer cloud model intercomparison study of the first ASTEX Lagrangian experiment. *Bound.-Layer Meteor.,* **93,** 341–380.

Browning, K. A., 1993: The GEWEX Cloud System Study (GCSS). *Bull. Amer. Meteor. Soc.,* **74,** 387–399.

Cuijpers, J. W. M., and P. G. Duynkerke, 1993: Large eddy simulation of trade wind cumulus clouds. *J. Atmos. Sci.,* **50,** 3894–3908.

Golaz, J.-C., V. E. Larson, and W. R. Cotton, 2002: A PDF-based model for boundary layer clouds. Part I: Method and model description. *J. Atmos. Sci.,* **59,** 3540–3551.

Harrington, J., and J. Verlinde, 2004: Mixed-Phase Arctic Clouds Experiment (M-PACE). U.S. Department of Energy Scientific Overview Document, 28 pp. [Available online at http://nsa.met.psu.edu/verlinde/mpace/sciencedoc.pdf.]

Holland, J. Z., and E. M. Rasmusson, 1973: Measurement of atmospheric mass, energy, and momentum budgets over a 500-kilometer square of tropical ocean. *Mon. Wea. Rev.,* **101,** 44–55.

Houghton, J. T., Y. Ding, D. J. Griggs, M. Noguer, P. J. van der Linden, X. Dai, K. Maskell, and C. A. Johnson, Eds., 2001: *Climate Change 2001: The Scientific Basis*. Cambridge University Press, 944 pp.

Kessler, E., 1969: *On the Distribution and Continuity of Water Substance in Atmospheric Circulation. Meteor. Monogr.*, No. 32, Amer. Meteor. Soc., 89 pp.

Köhler, M., 2005: Improved prediction of boundary layer clouds. *ECMWF Newsletter,* No. 104, ECMWF, Reading, United Kingdom, 18–22.

Kuang, Z., and C. S. Bretherton, 2006: A mass-flux scheme view of a high-resolution simulation of a transition from shallow to deep cumulus convection. *J. Atmos. Sci.,* **63,** 1895–1909.

Lappen, C.-L., and D. A. Randall, 2001: Toward a unified parameterization of the boundary layer and moist convection. Part I: A new type of mass-flux model. *J. Atmos. Sci.,* **58,** 2021–2036.

Larson, V. E., R. Wood, P. R. Field, J.-C. Golaz, T. H. Vonder Haar, and W. R. Cotton, 2001: Small-scale and mesoscale variability of scalars in cloudy boundary layers: One-dimensional probability density functions. *J. Atmos. Sci.,* **58,** 1978–1994.

Lewellen, W. S., and S. Yoh, 1993: Binormal model of ensemble partial cloudiness. *J. Atmos. Sci.,* **50,** 1228–1237.

Mellor, G. L., 1977: The Gaussian cloud model relations. *J. Atmos. Sci.,* **34,** 356–358.

Neggers, R. A. J., M. Köhler, and A. C. M. Beljaars, 2009: A dual mass flux framework for boundary layer convection. Part I: Transport. *J. Atmos. Sci.,* **66,** 1465–1487.

Nieuwstadt, F. T. M., and R. A. Brost, 1986: Decay of convective turbulence. *J. Atmos. Sci.,* **43,** 532–546.

Nitta, T., and S. Esbensen, 1974: Heat and moisture budget analyses using BOMEX data. *Mon. Wea. Rev.,* **102,** 17–28.

Rauber, R. M., and Coauthors, 2007: Rain in shallow cumulus over the ocean—The RICO campaign. *Bull. Amer. Meteor. Soc.,* **88,** 1912–1928.

Siebesma, A. P., and J. Teixeira, 2000: An advection–diffusion scheme for the convective boundary layer: Description and 1D results. Preprints, *14th Symp. on Boundary Layers and Turbulence,* Boulder, CO, Amer. Meteor. Soc., 133–140.

——, and Coauthors, 2003: A large eddy simulation intercomparison study of shallow cumulus convection. *J. Atmos. Sci.,* **60,** 1201–1219.

——, P. M. M. Soares, and J. Teixeira, 2007: A combined eddy-diffusivity mass-flux approach for the convective boundary layer. *J. Atmos. Sci.,* **64,** 1230–1248.

Sommeria, G., and J. W. Deardorff, 1977: Subgrid-scale condensation in models of nonprecipitating clouds. *J. Atmos. Sci.,* **34,** 344–355.

Stevens, B., and Coauthors, 2001: Simulations of trade wind cumuli under a strong inversion. *J. Atmos. Sci.,* **58,** 1870–1891.

——, and Coauthors, 2003a: On entrainment rates in nocturnal marine stratocumulus. *Quart. J. Roy. Meteor. Soc.,* **129,** 3469–3492.

——, and Coauthors, 2003b: Dynamics and Chemistry of Marine Stratocumulus—DYCOMS-II. *Bull. Amer. Meteor. Soc.,* **84,** 579–593.

——, and Coauthors, 2005: Evaluation of large-eddy simulations via observations of nocturnal marine stratocumulus. *Mon. Wea. Rev.,* **133,** 1443–1462.

Sundqvist, H., 1978: A parameterization scheme for non-convective condensation including prediction of cloud water content. *Quart. J. Roy. Meteor. Soc.,* **104,** 677–690.

Tiedtke, M., 1993: Representation of clouds in large-scale models. *Mon. Wea. Rev.,* **121,** 3040–3061.

Verlinde, J., and Coauthors, 2005: Overview of the Mixed-Phase Arctic Cloud Experiment (M-PACE). Preprints, *Eighth Conf. on Polar Meteorology and Oceanography,* San Diego, CA, Amer. Meteor. Soc., P1.14. [Available online at http://ams.confex.com/ams/pdfpapers/85743.pdf.]

Wyant, M. C., C. S. Bretherton, H. A. Rand, and D. E. Stevens, 1997: Numerical simulations and a conceptual model of the stratocumulus to trade cumulus transition. *J. Atmos. Sci.,* **54,** 168–192.